

$\text{CdS}_x\text{Te}_{1-x}$: bulk vapour growth, twin formation and the electrical activity of twin boundaries

This article has been downloaded from IOPscience. Please scroll down to see the full text article.

2002 J. Phys. D: Appl. Phys. 35 1997

(<http://iopscience.iop.org/0022-3727/35/16/314>)

View [the table of contents for this issue](#), or go to the [journal homepage](#) for more

Download details:

IP Address: 138.253.100.121

The article was downloaded on 30/06/2011 at 09:36

Please note that [terms and conditions apply](#).

CdS_xTe_{1-x}: bulk vapour growth, twin formation and the electrical activity of twin boundaries

K Durose¹, A J W Yates¹, A Szczerbakow², J Domagala²,
Z Golacki² and K Swiatek²

¹ Department of Physics, University of Durham, South Road, Durham DH1 3LE, UK

² Institute of Physics, Polish Academy of Sciences, al. Lotników 32/46,
PL-02-668 Warszawa, Poland

Received 2 May 2002

Published 6 August 2002

Online at stacks.iop.org/JPhysD/35/1997

Abstract

CdS_xTe_{1-x} has been used as a model substance to investigate crystal growth from the vapour, twinning phenomena and the electrical properties of grain boundaries. A self-selecting vapour growth method produced solid solutions of CdS_xTe_{1-x} ($x \approx 0.067$) with compositional uniformity of <2% of x (i.e. <0.0013) as determined by x-ray diffraction and photoluminescence spectroscopy. The CdS_xTe_{1-x} crystals were highly twinned. Statistical tests showed that the twin boundaries are spatially correlated. A model for twin formation based on nucleation and grain size development is proposed. Band bending at grain and twin boundaries in CdTe and in CdS_xTe_{1-x} was measured using the scanning electron microscope remote electron beam induced current technique. Boundaries in CdTe have downward band bending, but those in CdS_xTe_{1-x} have upward band bending. Decoration of grain boundaries with Te inclusions reduced the band bending effect in CdTe. It is postulated that the grain boundary passivation in CdTe/CdS solar cells is partly caused by enrichment of the grain boundaries in CdTe with CdS_xTe_{1-x}, and partly by the Te enrichment that occurs during processing.

1. Introduction

The solid solution CdS_xTe_{1-x} was considered as a potential opto-electronic material in the 1960s and 70s: in principle its energy gap is variable between 1.45 and 2.4 eV. However, CdTe and CdS adopt different crystal lattices and there is a wide miscibility gap.

In the present paper the motivation for working on CdS_xTe_{1-x} is three-fold:

- CdS_xTe_{1-x} is a model substance for the study of the vapour-phase crystal growth challenge of forming a homogeneous ternary solid solution from two binaries having disparate vapour pressures.
- CdS_xTe_{1-x} ($x < 0.2$) is a model substance for the study of twinning: CdTe is stable in the sphalerite lattice and its twin, CdS, adopts the wurtzite lattice at equilibrium but is only weakly stable with respect to the sphalerite lattice. Addition of a small fraction of CdS to CdTe to form a

solid solution can be expected to predispose the material further towards twinning.

- CdS_xTe_{1-x} ($x < 0.2$) is of current interest as it occurs as an important interfacial phase at the heterojunction of CdTe/CdS solar cells. It is known to modify optical absorption and has been postulated to influence the electrical junction by grain boundary diffusion of CdS into CdTe.

1.1. Properties of CdS_xTe_{1-x}

Properties of CdS_xTe_{1-x} relevant to this paper are now briefly reviewed. Throughout this paper the anion fraction x is defined such that $0 < x < 1$. Here, percentages are reserved for the description of uniformity or error in x . The T– x diagram for the solid solution is reported by Ohata [1]. CdTe-rich compositions adopt the sphalerite lattice, while CdS-rich ones adopt the wurtzite one. Within these mono-phase regions Vegard's law is followed as reported by Ohata [1], and more

recently by Wood [2]. The miscibility gap is temperature dependent and extends over >80% of the range of x , although metastable thin films have been made with compositions in the miscibility gap. The band gap— x diagram was recorded by Ohata [3], and Jensen [4] reports a synthesis of data recorded by other authors. There is severe bowing with the band gap reaching a minimum at $x \approx 0.2$. There is very great scatter in the reported data, so much so that little is lost by approximating a linear relationship between band gap and x ($x < 0.2$) rather than the usual polynomial.

$\text{CdS}_x\text{Te}_{1-x}$ was first postulated to exist in CdTe/CdS solar cells to explain light blocking observed in spectral response measurements of cell performance [5]. Compositions with $x < 0.2$ are thought to block light from entering the absorber. The thin film solar cell literature now abounds with physical studies of interdiffusion in this polycrystalline system. Notably, McCandless [6] and Lane [7] have demonstrated by combinations of x-ray diffraction (XRD), diffusion measurements and modelling that CdS diffuses into the CdTe preferentially along the grain boundaries. The grain boundaries near to the heterojunction therefore have CdTe-rich compositions of $\text{CdS}_x\text{Te}_{1-x}$. It is known that processing conditions promoting excessive interdiffusion lead to dissolution of the heterojunction. Nevertheless, it is found empirically that some degree of interdiffusion is a requirement for the fabrication of efficient solar cell devices. It has been postulated but not proven that the $\text{CdS}_x\text{Te}_{1-x}$ compositions influence current transport at the heterojunction and in the absorber.

1.2. Crystal growth aspects

Vapour growth of homogeneous ternary solid solutions of materials comprising two binaries having a wide difference in vapour pressures presents a particular problem. Also many vapour growth configurations do not avoid contact of the growing crystal with its container. One method that addresses these problems is the self-selecting vapour growth (SSVG) method. In SSVG the temperature difference between the source and the growing crystal that promotes growth is low (typically 2°C) and is provided by the optical radiation field of a tube furnace. For a horizontal tube furnace having cool end caps, geometric analysis of the radiation field shows the centre line of the furnace to be cooler than the near-wall parts. Hence material placed in a capsule in such a furnace undergoes transport from the hot wall side towards the furnace tube axis, as shown in figure 1. In practice the charge material can be polycrystalline granules. Transport occurs from beneath the charge and crystal growth occurs on top. This process can continue indefinitely—with the grown crystal eventually sinking to occupy the charge position and hence becoming the source of material for transport. This process of ‘re-cycling’ actively refines the polycrystalline charge to a single crystal. It is presumed that the single crystal arises since it represents a fast growing orientation that out-grows the slow ones.

A further description of the SSVG process is given by Szczerbakow [8] and is the subject of a review [9]. The method has long been used for the growth of iv–vi compounds [9] and was extended for use with the ii–vi binaries CdTe [8] and (with a vertical configuration) ZnTe [10]. The

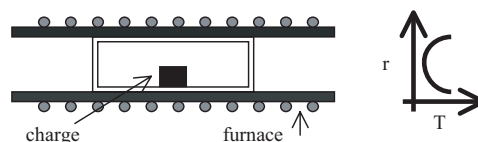


Figure 1. Schematic diagram of the SSVG method. The polycrystalline charge is sublimed from the hot furnace wall and the vapour crystallizes on the cool upper surface of the charge. The process can continue indefinitely—the charge is eventually replaced by grown crystalline material that is itself re-sublimed to condense as further new growth.

ii–vi solid solutions $\text{CdZn}_x\text{Te}_{1-x}$ [8] and $\text{CdSe}_x\text{Te}_{1-x}$ [11] were successfully grown. For $\text{CdSe}_x\text{Te}_{1-x}$ the considerable vapour pressure differences between CdSe and CdTe [12] were no barrier to crystal growth by SSVG. Since CdS and CdTe have similarly disparate vapour pressures, it is expected that the SSVG method may also be appropriate for the growth of $\text{CdS}_x\text{Te}_{1-x}$ solid solutions. Moreover similar growth conditions might be used for both.

1.3. Twinning in vapour-grown crystals

Structural defects in the ii–vi materials are reviewed by Durose [13]. Both the close packed lattices (sphalerite and wurtzite) and all of the planar defects (stacking faults, polytypes and twins) may be considered in terms of the stacking sequences of close packed planes. The possibility of two types of twins distinguished by mirror symmetry was raised by Holt [14], and it was demonstrated experimentally that the low energy ‘ortho-’ type occurs for CdTe [15]. This is the $\Sigma = 3$ first-order twin and has $\{111\}$ boundaries containing no disrupted bonds. Often these long straight (low energy) boundaries are terminated by incoherent or ‘lateral’ boundaries. Coincidence site lattice modelling shows that lateral twin boundaries must contain (electrically active) wrong bonds for geometric reasons. Predisposition of a material to planar faulting may be understood in terms of its relative stability in the sphalerite and wurtzite lattices [16, 17]. CdTe is relatively stable in the sphalerite lattice but is unstable enough to permit twinning and stacking faults but not polytypism or dimorphism. CdS is unstable, dimorphic and prone to polytypism. Hence it may be expected that addition of a small fraction of CdS to CdTe in a solid solution will increase the likelihood of twin formation in $\text{CdS}_x\text{Te}_{1-x}$ over CdTe.

Although it can be understood from lattice stability arguments whether or not a material is predisposed to planar faulting, there is no conclusive proof as to the exact causes of twinning events in vapour-grown bulk crystals.

For the case of oriented epilayer growth, a kinetic mechanism has been formulated that is based on the difference in growth rate between matrix and twinned surfaces. This provides a basis for predicting whether a particular growth orientation will either promote, block or be neutral for twin formation. Twinning is promoted during growth if a twin band presents an orientation to the growth surface that is faster growing than the matrix. Should the converse be true, twinning is suppressed. For a case where the growth rates are equal, the twin and matrix orientations may be present in equal volumes. This scheme is successful in predicting the

occurrence and distribution of twins in vapour-grown epitaxial ii–vi semiconductors.

For Czochralski-grown crystals of iii–v semiconductors, Hurle [18] extended Voronkov's free energy assessment of step formation at the triple phase (S–L–G) boundary [19] to include twinning phenomena. Hurle describes the conditions that might promote the formation of a twin nucleus at such a step. Using the available thermo-chemical data it was demonstrated that surface energy may in principle drive twinning in a range of semiconductors. No such quantitative model has been formulated for the rather different physical situation of vapour growth.

A second energetic driver for twinning in bulk vapour growth has been argued qualitatively by Cutter for the cases of ZnSe and Zn(S,Se) [20]. Cutter *et al* invoke twinning as a means of preserving the overall convex shape of the growth front—whereas it may otherwise have a tendency to become sloping. The energetic advantage of this is not discussed; perhaps the authors had in mind that a convex growth front has minimum free energy, and that there is an energetic advantage in maintaining that via the following twinning mechanism. The work noted that (a) for the ii–vi semiconductors the 'B' surfaces generally grow faster than the 'A' faces, and (b) the 'ortho-twin' relationship [14] causes an 'A'-oriented growth (matrix) surface to transform to a 'B' surface on a twin band. Cutter suggests local slowing of a growth front (to minimize the growth front energy) by twinning as a possible mechanism of twin formation [20]. However, they point out that this only accounts for twins intersecting the growth front, while in practice many other twin orientations were observed in vapour-grown Zn(S,Se).

As an alternative energy-driven process, Cutter [20] considered deformation twinning, and described the crystallography of the necessary stacking-order changes resulting from the passage of 1/6{211} partials over successive {111} planes. Neither specific dislocation sources, nor an energetic comparison of twin and slip deformation mechanisms were considered. In an experimental study of deformation twinning, Vere [21] subjected [123] oriented bars of CdTe to tensile test at temperatures up to 500°C. Although no stress-induced twinning could be induced, those authors point out that the deformation twinning mechanism cannot be ruled out on that basis alone.

1.4. Electrical properties of extended defects

The charge state and fields surrounding extended defects in semiconductors, i.e. their electrical activity, is important as it influences the performance of minority carrier devices such as light emitters and detectors: electrically active defects can act as recombination centres. CdS_xTe_{1-x} is known to occur as an important interfacial phase in polycrystalline CdTe/CdS solar cells. Although the interdiffusion has been empirically associated with device performance, no evidence exists at the present time to support any mechanism for passivation.

The origins of grain boundary electrical activity are thought to be two-fold. It may arise from grain boundary bonding conditions or from some type of impurity or point defect segregation. Either might give rise to a sheet of positive (or negative) charge that will generate a local electric field and hence downward (or upward) band bending near the grain

boundary. More complex potential profiles might be expected to arise from other local dopant concentration profiles.

For the case of p-CdTe/n-CdS solar cells, most photocurrent collection is from the CdTe absorber, the minority carriers being electrons. From the observation that such cells operate with high photocurrents it may be inferred that the CdTe grain boundaries are electrically passive, i.e. there is a potential barrier preventing electrons from recombining at them. Some evidence for upward band bending at grain boundaries in device CdTe comes from two sets of experiments.

Firstly, Woods *et al* [22, 23] have used a combination of in-plane conductivity and impedance spectroscopy measurements to infer the band diagram in figure 2(a). A combination of electron beam-induced current (EBIC) measurements in their cross-section, plan view, temperature and beam current dependent forms was used by Galloway [24, 25] to infer the band diagram in figure 2(b). Both schemes would act to repel minority carrier electrons as they approached the grain boundary, but the models differ in points of detail.

1.5. The R-EBIC method

In this paper, the scanning electron microscope (SEM) technique of R-EBIC ('remote' EBIC) is used to characterize grown-in boundaries in CdTe reference crystals and in CdS_xTe_{1-x}. Application of some of the many variants of the EBIC method to CdTe solar cells are described in the review by Edwards [25]. However, the R-EBIC method described below has only been applied to CdTe related materials in one preliminary study by the present authors [17].

Figure 3 shows the R-EBIC circuit. The sample is connected by two conductive contact which should be 'remote' from one another by many diffusion lengths, in practice several millimetres. The signal collected by the amplifier may be recorded as an image or a line scan. Image contrast arises from two sources:

- Resistive contrast.** As the beam current I_b impinges upon the sample, the signal measured is the fraction of I_b flowing to the earth via the amplifier: the sample acts as a current divider. If the sample has uniform resistivity, a ramp of uniform signal gradient is observed, one contact being black, the other white. Should the sample contain a resistive barrier that supports a potential drop, then a terraced form of contrast results [26, 27].
- Peak and trough contrast.** This is superimposed on resistive contrast if the sample contains an electrically

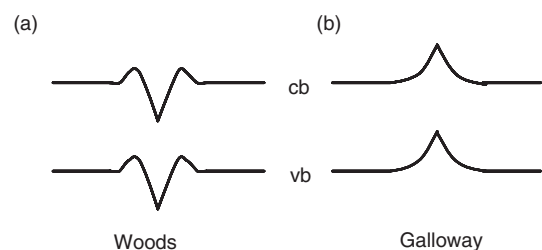


Figure 2. Schemes for the potential distribution near to grain boundaries in CdTe absorber layers in CdTe/CdS solar cells determined from the experiments. (a) Woods, (b) Galloway.

active defect that is capable of separating electron–hole pairs, i.e. injected carriers. Depending on the sign of the local field at the defect, the additional signal collected can either add to or subtract from the resistive contrast signal.

The peak and trough contrast has been described quantitatively in [27] (equation (8)) but that work contains a minor error. We believe the correct expression to be

$$I_{R-EBIC} = \eta \frac{\delta}{d} G I_b = \eta \frac{\delta}{d} \frac{V_b I_b}{\varepsilon_i}$$

where I_{R-EBIC} is the collected current (A), η is efficiency of charge collection, δ is drift length of the injected carriers in the local field (m), d is sample length (m), G is the generation electron–hole pairs per beam electron, I_b is beam current (A), V_b is beam voltage (V) and ε_i is energy (eV) per electron–hole pair.

An example of the combined R-EBIC contrast arising from grain boundaries with both up and downward band bending is shown in figure 3. This figure also serves to illustrate the current convention used in the present paper. Conventional currents are used throughout, i.e. positive charge carriers constitute a positive current, electrons give a negative current. For all R-EBIC images and line-scans presented, the bright (high positive current) contact is shown on the left and the dark (large negative current) is shown on the right. Using these conventions and considering the electron beam to be scanned from the left to right of the figures, it can be seen that grain boundaries with upward band bending give bright \rightarrow dark peak and trough contrast, while downward band bending gives dark \rightarrow bright contrast.

2. Experimental

Crystal growth was undertaken in a sealed ampoule containing the nominal starting composition of 95% CdTe and 5% CdS. This was maintained at 825°C in the central zone of a horizontal tube furnace for a total growth period of 10 days.

Composition and compositional uniformity were measured by XRD (by monitoring lattice parameter via the 004

reflection), by photoluminescence (PL) spectroscopy at 1.8 K with an excitation energy of 2.54 eV, and with standardless energy dispersive x-ray analysis (EDX) using a JSM IC848 SEM equipped with a PGT x-ray detector and Avalon software.

For the defect selective etching of twins, the following etchants were tested: bromine in methanol, Inoue's E reagent [28] (acidified dichromate), saturated FeCl₃ solution and chromic acid. The chemical compositions are shown in table 3.

The positions of 200 twin boundaries were recorded from a montage of SEM micrographs and listed to a file for statistical analysis. Numerical routines for determination of the nearest neighbour distribution coefficient, for comparison of the distribution with a Poisson distribution and for generating a correlation function were written in Salford FORTRAN. In order to assist with interpreting the outcomes, three sets of synthetic data were generated by numerical means and subjected to the same tests. These were (a) a random data set, (b) a clustered data set and (c) a part random, part clustered 'semi-clustered' data set.

Both vapour-grown CdTe [29] and CdS_xTe_{1-x} grown in this study were examined by R-EBIC. For CdTe the contacts were evaporated Au dots. For CdS_xTe_{1-x}, contacts made with Au coated needles (mounted on an Ernst Fullam micromanipulator) were adequate. The microscopy was done in a JSM IC848 SEM with a dedicated Matelect ISM5 current amplifier.

3. Results and discussion

3.1. Growth outcomes

During 10 day growth runs, boules like that shown in figure 4 were produced. The growth surfaces were faceted and shiny, and had mainly {110} orientations. The boules were predominantly single grains with a high density of twins running along their growth axes. 004 rocking curves recorded from cleaved facets indicated severe mosaicity with the mosaic blocks being tilted over a range of 1°. Each mosaic block had a rocking curve half width of $\leq 0.1^\circ$. The boule shown in figure 4 was selected for detailed characterization as described below.

3.2. Composition and compositional uniformity

3.2.1. Determination of composition using x-ray lattice parameter (Vegard's law). High resolution XRD was used to

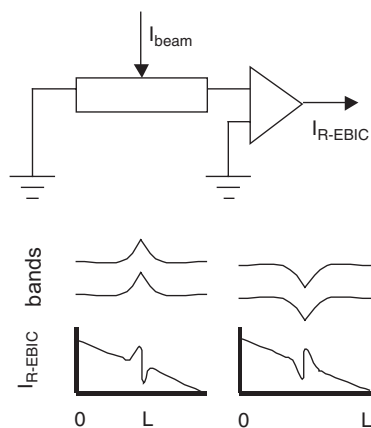


Figure 3. Circuit used in R-EBIC investigations of grain boundaries and the forms of the results expected for upward (left) and downward (right) band bending. For the convention used in this work the form of the peak and trough contrast read from left to right indicates the sense of the band bending. Conventional currents (negative currents for electron flow) are used.

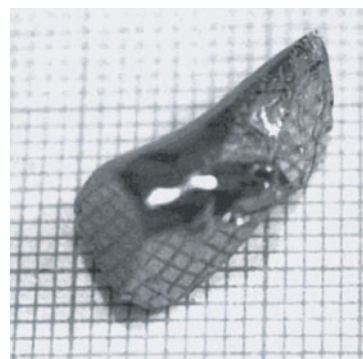


Figure 4. Photograph of a boule of CdS_xTe_{1-x} grown by the SSVG process. The growth was in the direction parallel to the axis of the boule.

determine the composition and compositional variation over a 10 mm slice of the sample. Linear variation of the lattice parameter of a binary material with composition is given by Vegard's law and for CdS_xTe_{1-x} this can be applied to each monophasic region, in this case the compositional extent of the cubic phase, i.e. $0 < x < 0.2$. This was first determined by Ohata [1] but more recently by Wood [2] with an error analysis. Wood's data is $a_{\text{cubic}}(\text{nm}) = c - mx$ where c is the lattice parameter of CdTe. The values of m and c are 0.07040 ± 0.00358 , 0.64912 ± 0.00045 (nm), respectively.

The samples studied in this paper had considerable mosaicity and this lead to multiple overlapping 004 peaks in the HRXRD spectra. This introduced errors of 4×10^{-6} nm into the lattice parameter determination.

Experimentally, the average lattice parameter a was 0.64454 nm with a spread of values over the slice of ± 0.00005 nm. From Vegard's law this gives an average composition of $x_{\text{av}} = 0.0651$ and a spread in x values of ± 0.0007 . Expressed as a percentage of the average composition this spread is 1.1%. It is now shown that these measurements are precise but not accurate.

In order to assess these values, the errors in x determination (α_x) were calculated by adding error terms due to a (α_a), m (α_m) and c (α_c) in quadrature in the usual way. Firstly, the error in the calculation of absolute values of x from lattice parameter a is evaluated. The errors in each term are shown in table 1. The resulting error in x for the average composition for the samples studied in this paper is 0.007. This represents a percentage error of $100 \times 0.007/0.0651 = 11\%$, the largest term in this uncertainty arising from the error in the value of m which is itself 5%. From this, it may be concluded that absolute values of the fractional composition value x in the range of interest can only be determined with an accuracy of $\pm 11\%$.

Most of the uncertainty in x determination arises directly from uncertainty in the values of the Vegard coefficients, rather than from any failure of Vegard's law itself. It therefore follows that composition measurement using the x-ray method in this case is precise but not accurate. This can be illustrated by setting the errors in m and c to zero while assuming that the error arises solely due to error in the measurement of a (4×10^{-6} nm), as shown in table 1. For the average composition this returns a value of $x = 0.0651 \pm 2 \times 10^{-5}$, i.e. a percentage error of $100 \times 2 \times 10^{-5}/0.0651 = 0.03\%$. Hence this error in *relative* compositional variation (0.03%) is considerably less than the measured variation in composition itself (1.1%). It may therefore be inferred that the composition of the crystal varies by $\pm 1.1\%$ of the value of x .

3.2.2. Determination of composition using PL spectroscopy. For determination of x using PL energies, the constraints on accuracy and precision are similar to those for x-ray measurements. The (parabolic) relation between band gap (E_g) and x has been determined by Ohata [3] and others. Jensen [4] shows a composite of the published experimental results for the region $0 < x < 0.2$. There is a very great scatter of the experimental data and no further loss of accuracy results from making a linear approximation:

$$E_g(\text{CdS}_x\text{Te}_{1-x}) = E_g(\text{CdTe}) - 0.5x \quad (\text{band gaps in eV})$$

PL does not give band gaps directly but near band-edge features have energies that are close to the band gap. By assuming that the difference in energy between the near-edge emission energy and the band gap energy to be invariant with x , the x values can be calculated directly.

Near-edge features in PL spectra in CdTe [30] occur at 1.591 eV at 1.6 K. In the present experiments, shallow luminescence features recorded over a 10 mm slice of a CdS_xTe_{1-x} crystal (10 values) had an average of 1.5565 eV with a spread of 0.00073 eV (1 SD). Some of the spectra are shown in figure 5. These values correspond to $x = 0.0691 \pm 0.0015$ (1 SD), i.e. a compositional spread of $100 \times 0.0015/0.0691 = 2.1\%$ of the value of x .

The principal error in determining the x values arises from the spread of experimental reference data (i.e. the coefficient of x , in the above equation). Determination of x is therefore limited in accuracy to $\pm 28\%$ of the value of x . However, as for Vegard's law, the underlying relationship is secure and hence the relative measurement x can be established with a precision limited by the spectrometer resolution. Such relative measurements have an error of $\pm 0.2\%$ of the value of x . Since this error is small compared to the spread of x values observed, the compositional uniformity can be known accurately. For this sample, the compositional uniformity determined from luminescence is therefore $\pm 2.1\%$ of the value of x .

3.2.3. Determination of composition using x-ray microanalysis. EDX spectra from eight points over a distance of 7 mm on a cleaved slice of the CdS_xTe_{1-x} boule were recorded and the composition was determined by standardless ZAF correction. The average composition values with their standard deviations are as follows: S = 0.036 (SD = 0.0013 or 3.7% of x), Te = 0.431 (SD = 0.0025 or 0.6% of x) and (Te + S) = 0.468 (SD = 0.0024 or 0.5% of x).

From these values $x = \text{S}/(\text{S} + \text{Te}) = 0.077$ (SD = 0.003 or 3.7% of x). Error arising from the analysis method and the

Table 1. Error calculations for the determination of composition from lattice parameter measurements.

Lattice parameter a (nm)	Error in c (α_c)	Error in m (α_m)	Error in a (α_a)	Composition (x)	Error in x (α_x)	Percentage error in x ($100\alpha_x/x$)
0.64454	0.00045	0.00358	4×10^{-6}	0.0651	0.007	11
0.66454	0.0	0.0	4×10^{-6}	0.0651	2×10^{-5}	0.03

The errors were added in quadrature. The accuracy of absolute calculations of x shown in the first row is limited by uncertainty in the *measured* Vegard coefficient c . Nevertheless, as it can be assumed that Vegard's law does not itself have significant uncertainty, the precision of *relative* measurement of x is high. Hence, while the absolute composition cannot be known with great accuracy, the compositional uniformity can accurately shown to be 1.1%.

ZAF correction cannot easily be quantified without reference samples unavailable to this work. Nevertheless, an indication of error can be gauged by noting the following:

- the average S + Te fraction deviates from 0.500 by 0.032 and,
- the standard deviations of the S and Te determinations differ significantly (3.6% and 0.6%, respectively), while if self-consistent they would be equal.

Owing to these non-quantifiable systematic errors, in this paper the microanalysis values of $x = 0.077 \pm 0.003$ (a variation of 3.7% of x) are taken as indicators only: they are roughly consistent with the results from x-ray and luminescence determinations but are less accurate and less precise.

3.2.4. Summary of composition measurement results. Both the x-ray and PL methods have errors arising from: (i) the measurement precision itself, and (ii) the errors in the reported measurements of the fundamental relations between composition and both lattice parameter and band gap. By considering both sources of error, the error in the absolute determination of composition (x) can be calculated (percentage error in absolute value of x). The resulting errors are up to 28% of x as shown in table 2. In order to make a meaningful measurement of compositional uniformity, the fundamental relationships must be

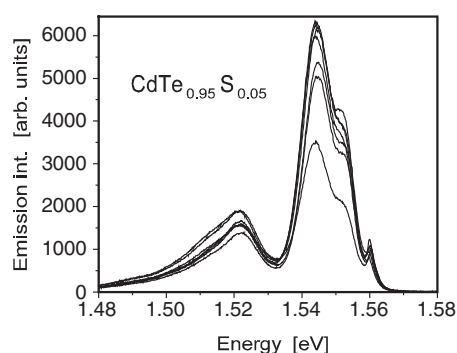


Figure 5. A selection of PL data recorded at intervals on a cleavage facet of a slice of $\text{CdS}_x\text{Te}_{1-x}$ at 1.8 K. The close correspondence of the energies of the peaks recorded from different positions on the boule indicates that the composition is very uniform. An analysis of the compositional uniformity is presented in the text.

Table 2. Summary of composition determinations, compositional uniformity and the errors of each.

Method	x	Error in absolute value of x (%)	Measured variation in x over a slice (%)	Error in relative value of x (%)
XRD	0.0651	11	1.1	0.03
PL	0.0691	28	2.1	0.2
EDX	0.077	Not quantified	3.7	Not quantified

considered accurate and only (i) above is considered. This allows calculation of the percentage error in the relative value in x —which is up to 0.2% of x —and is sufficiently low to allow measurement of compositional uniformity. For standardless EDX the errors are not quantifiable in a simple way.

From the XRD and PL it may be concluded that the composition is $x = 0.067$ with an uncertainty of 11–28% of this value. More importantly the variation in x over a slice is found to be 1–2% of x , this being measured with a precision of 0.03–0.2% of the value of x . This is a favourable result in terms of the uniformity of such a ternary compound.

3.3. Twinning

3.3.1. Observations of twinning. The results of the etch trials are shown in table 3. Although Inoue's E reagent and bromine/methanol work well for CdTe, they leave a coating on CdS_{Te} and this makes them unusable for chemical polishing of the mixed crystal. Chromic acid was however effective as a combination polish and defect revealing etchant that delineates twin boundaries on surfaces that had been polished with 1 μm grit—as shown in figure 6. Under favourable tilting conditions, the twin bands were visible owing to crystallographic contrast as seen in the figure. However, it was generally possible to see more twin boundaries in secondary electron mode.

Generally the twins in these boules were in the form of complete lamellae (sheets) that ran parallel to the growth axis for the full length of the boule and intersected the growth surface. The twins are hence embedded in the host lattice (matrix) orientation. The ratio of the volume of the crystal that is occupied by twin to that occupied by the host lattice is defined as the twin : matrix ratio. It can be evaluated by measuring the ratios of the areas of twin and matrix on the etched surface of the crystal. In this paper, the ratio was determined over a sample of 200 twin boundary positions from a continuous montage of secondary electron micrographs and a value of 39% : 61% was determined. The method of calculation used the twin boundary positions and assumed that each boundary crossed represented a transition between the matrix and twin orientations. Errors may arise from this procedure if twin bands exist which are not resolved by the etching and recording process: it could be possible to incorrectly assign a group of twin bands. For example, were the widest twin band recorded be mis-assigned then the error in this case would be 11%. For the purpose of this paper it is relevant to note that the twin : matrix ratio is not significantly biased in favour of either the twin or matrix orientations.

Figures 7–10 show the experimental and the synthetic twin position data alongside graphs showing the comparison with a Poisson distribution and the autocorrelation analysis. Numerical data from the analysis is shown in table 4.

Table 3. Etchants tested and their action on Cd(S,Te).

Etchant	Composition	Action
Inoue's E reagent	4 g $\text{K}_2\text{Cr}_2\text{O}_7$ + 10 ml HNO_3 + 20 ml H_2O	Smooth surface but stained
Bromine/methanol	2% bromine + 98% CH_3OH	Smooth surface but stained
FeCl_3	Saturated FeCl_3 in H_2O	Smooth but stained
Chromic acid	300 g Cr_2O_3 + 1391 ml H_2O + 70 ml H_2SO_4	Bright clean surface with twin boundaries revealed

Next, the experimentally observed distribution of twins is assessed using each analysis method in turn and with reference to the synthetic reference data.

- (a) Visual inspection. The experimental data (figure 7(a)) bears qualitative resemblance to the semi-clustered data (figure 10(a)).
- (b) Nearest neighbour analysis (see table 4). When $R_n \approx 1$ the points approach a random distribution (see figure 8(a)), while when R_n is small and positive, the distribution is clustered as shown in figure 9(a) for which $R_n = 0.191$. The experimental data is similar to the synthetic semi-clustered data in figure 10(a).

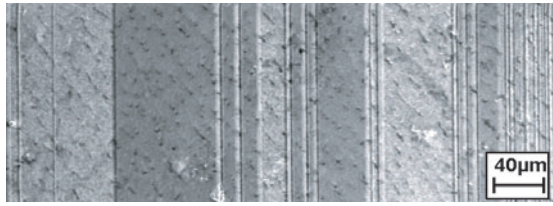


Figure 6. Backscattered SEM micrograph of twin bands on an etched surface of CdSTe.

Both show behaviour that is partly clustered and partly random.

- (c) Comparison with a Poisson distribution. As expected the synthetic random data fits the Poisson curve with >99% certainty (figure 8(b)). Clustered data (figure 9(b)) fits poorly while the experimental data shows a behaviour intermediate between that of random and clustered but similar to the semi-clustered.
- (d) Autocorrelation function. For random data (figure 8(c)) the correlation function is very nearly 1.0 for all distances, except where very high noise is expected due to the lack of data points (i.e. for spacing >0.9). For the synthetic clustered data, a peak can be seen at 0.4 which this represents the separation of the clusters. (The peak at a spacing of 0 represents intra-cluster relationships.) The experimental data shows evidence of clusters with separations of 0.4, 0.75 and 0.9. Anti-clustering (empty spaces) are represented by minima, but are not so pronounced as in the plot for the synthetic clustered data (figure 9(c)).

All of the statistical tests indicate that the twins in the CdS_xTe_{1-x} are largely correlated (perhaps 60%) with the remainder being randomly distributed.

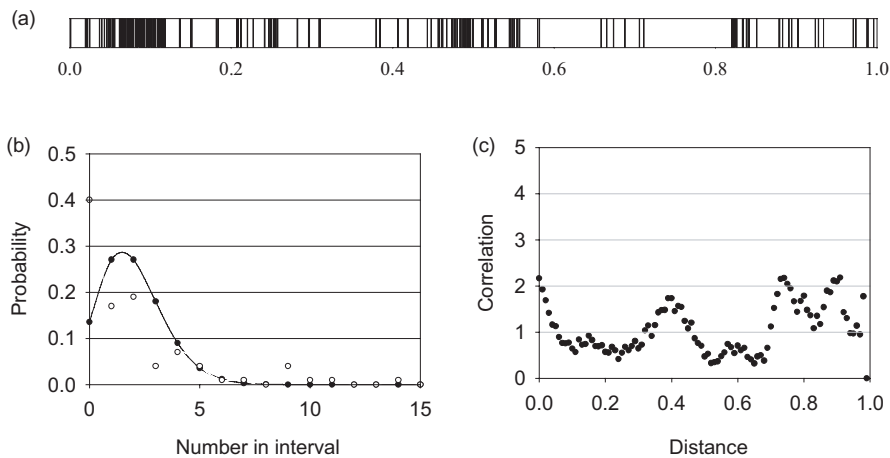


Figure 7. Analysis of twin boundary distributions: experimental data. (a) Twin boundary distribution on normalized unit field. (b) Comparison of distribution histogram with a Poisson distribution. (c) Correlation function analysis on normalized unit field.

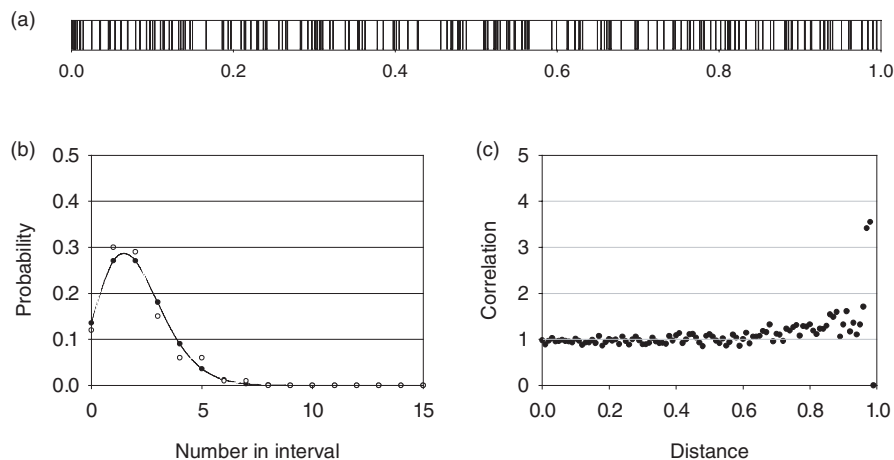


Figure 8. Analysis of twin boundary distributions: random data (synthetic). (a) Twin boundary distribution on normalized unit field. (b) Comparison of distribution histogram with a Poisson distribution. (c) Correlation function analysis on normalized unit field.

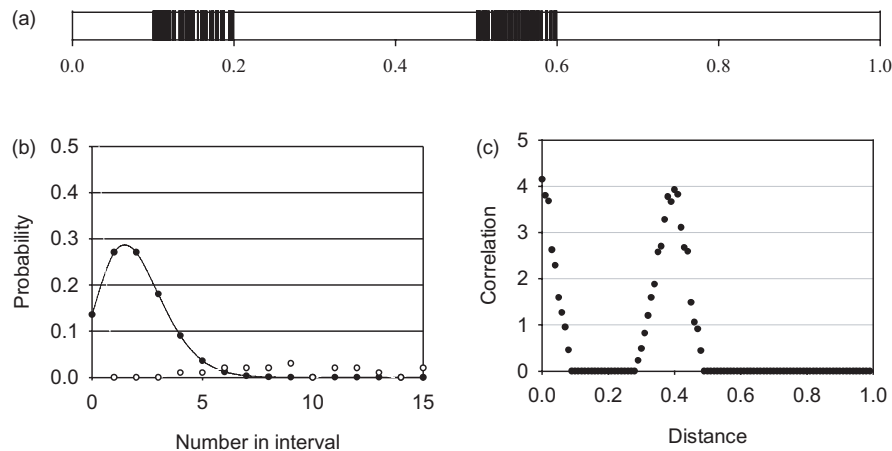


Figure 9. Analysis of twin boundary distributions: clustered data (synthetic). (a) Twin boundary distribution on normalized unit field. (b) Comparison of distribution histogram with a Poisson distribution. (c) Correlation function analysis on normalized unit field.

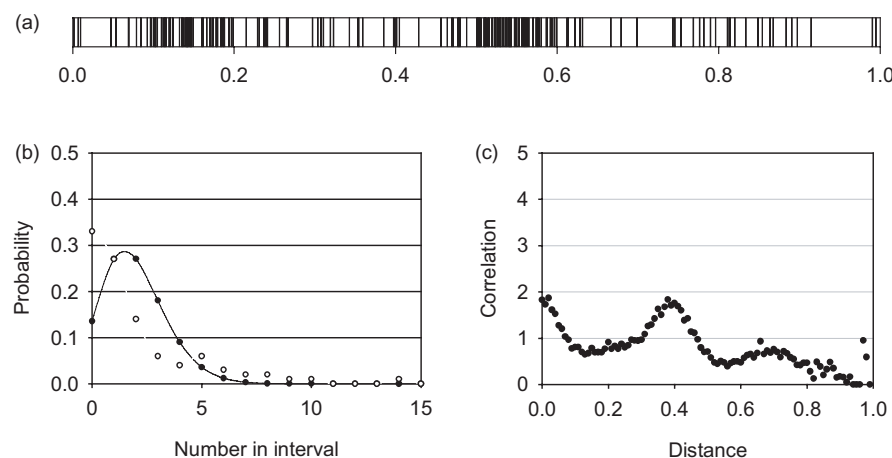


Figure 10. Analysis of twin boundary distributions: semi-clustered data (synthetic). (a) Twin boundary distribution on normalized unit field. (b) Comparison of distribution histogram with a Poisson distribution. (c) Correlation function analysis on normalized unit field.

Table 4. Numerical results of statistical testing of the experimental and synthetic distributions of twin boundaries.

Data set	Distribution parameter R_n	χ^2	d.o.f.	Probability of random data (%)
Experimental data	0.589	30.57	12	<1
Random points (synthetic)	1.001	1.81	12	>99
Clustered points (synthetic)	0.191	56.43	8	<0.1
Semi-clustered points (synthetic)	0.934	27.26	14	<0.1

The nearest neighbour distribution parameter is described in the text. The χ^2 data tests whether the distributions tested could arise from random positioning alone.

3.3.2. Twinning—interpretation of current observations. In this paper the following has been observed:

- (a) Growth is free from the walls.
- (b) The growing crystal nucleates and rests on an initially polycrystalline source—during the process of crystal

growth the polycrystalline charge is refined to a single crystal with twins.

- (c) Twinning usually occurred on one of the four possible sets of $\{111\}$ planes, this being the set oriented so as to be closest to being parallel to the growth axis.
- (d) The twins are lamellar and propagate for the full length of the boule.
- (e) The twin boundary positions are 60% correlated and 40% random.
- (f) The twin : matrix ratio is not significantly weighted to twin or matrix orientations.

First, the possibility of deformation twinning is considered. Since growth takes place free from the walls, stress can only arise from the ‘seed’/crystal interface or from inside the boule itself by differential thermal contraction. No simple geometric scheme can be devised that projects stress onto the vertical $\{111\}$ plane in the required $\langle 211 \rangle$ direction required for deformation twinning.

Second, the origin of twins in the SSVG process is considered from the standpoint of the more general process of grain size development that is characteristic of the process itself.

Here twins are considered as a special case of grain boundaries that are straight, have high symmetry and low energy.

Grain nucleation and development in the SSVG process occurs in two interactive stages:

- (a) Initial growth is essentially by seeding onto a granular substrate. Grain boundary relationships of all types are nucleated by the coalescence of adjacent grains or by the propagation of pre-existing relationships from substrate grains. Individual 'bad' grains may nucleate clusters of grain boundaries, including clusters of twin boundaries.
- (b) Grain size increases as growth proceeds by one or more of the following mechanisms which are discussed with regard to grain and twin selection or elimination.
 1. Growth rate-driven auto-selection. The grains having the fastest growth rate are selected at the expense of the slower ones (i.e. the model by which SSVG has been assumed to operate. While this may select grains, the mechanism will not eliminate twins if the growth axis is the non-polar [110] direction, for which twin and matrix both have $\langle 110 \rangle$ orientation and hence equal growth rate. For SSVG, [110] is a frequently observed growth surface.
 2. Classical grain growth. Grain boundaries having curvature participate in grain growth, the rate of which is governed by $1/r$ (inverse radius) terms. The driving force is minimization of the total boundary energy. Straight grain boundaries, i.e. $\{111\}$ twin boundaries, cannot participate. Experimentally the cast-recrystallize-anneal process of CdTe synthesis and crystallization causes grain growth, but twins cannot be eliminated by annealing [31].
 3. Grain size development during additive vapour growth processes. Cousins [32,33] describes a simple computer model of vapour growth on a polycrystalline template: species arrive at a surface, migrate and stick at strong bonding sites. When the sticking site is adjacent to a grain boundary, the designation of the attaching species is made on the nearest neighbour bonding criteria. Hence grain growth arises from statistical fluctuations. For geometric reasons [32], species arriving near straight boundaries can only belong to the grain where they attach: there is no mechanism by which straight boundaries (twin boundaries) can migrate in this model.

All of the observed features in twin propagation in otherwise single crystals refined from polycrystalline source material are compatible with the above nucleation/grain size development model (a and b), irrespective of the mechanism (1–3) by which the grain size develops during the SSVG growth.

3.4. Electrical activity of grain and twin boundaries in CdTe and CdS_xTe_{1-x}

3.4.1. R-EBIC of CdTe reference samples. Figures 11 and 12 show a typical R-EBIC micrograph and line scan for a randomly oriented high angle grain boundary in bulk CdTe. Of the 15 such grain boundaries examined, all showed the dark → bright sense of contrast. This is consistent with



Figure 11. R-EBIC image of contrast from a high angle grain boundary in bulk CdTe showing dark → bright contrast consistent with downward band bending.

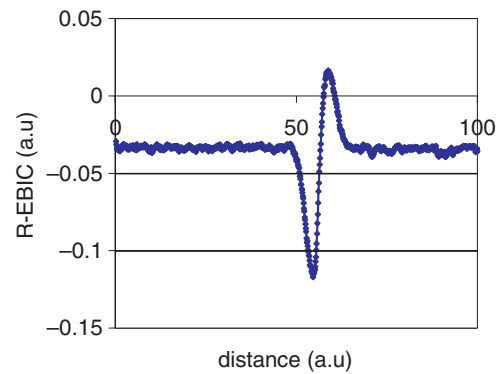


Figure 12. Line scan of the R-EBIC contrast in figure 11.

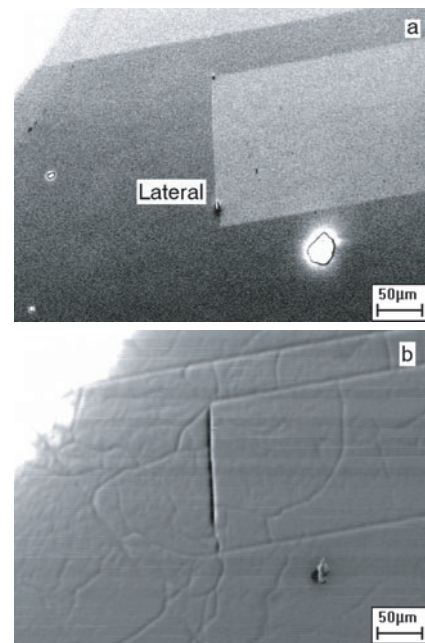


Figure 13. A $\Sigma = 3$ twin band in CdTe with coherent (parallel) twin boundaries, a lateral boundary (marked L) and a Te inclusion (marked Te). (a) backscattered SEM image, (b) R-EBIC image showing bright → dark contrast at all boundaries and also at a network of dislocation boundaries not visible in (a).

downward band bending as shown in figure 3. No grain boundaries with the opposite sense of contrast were seen in the samples studied.

Figure 13 shows a CdTe slice containing a $\Sigma = 3$ twin band. Its parallel $\{111\}$ coherent boundaries are terminated at a

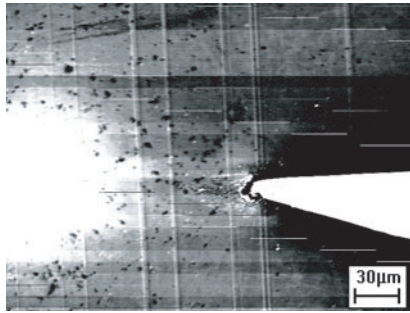


Figure 14. R-EBIC image of vertical twin boundaries in $\text{CdS}_x\text{Te}_{1-x}$ showing contrast with bright \rightarrow dark sense. (The horizontal features are noise.)

lateral (incoherent) twin boundary. The latter is decorated by a Te inclusion as is common in this material [15]. In the R-EBIC image (figure 13(b)) both the coherent and lateral boundaries have dark \rightarrow white contrast. Also a network of sub-grain boundaries (polygonization dislocation walls)—also seen in dark-bright contrast—is revealed. These contrast observations are consistent with there being downward band bending at all of these defects. Finally, the Te inclusion at the lateral twin was seen to be associated with reduced R-EBIC contrast compared to the boundary itself. This effect was also seen on grain boundaries and is consistent with locally reduced band bending.

In all of the observations of R-EBIC contrast in CdTe, there was little evidence of terrace type contrast. This is presumed to be because the contacts are resistive, so making the fraction of voltage dropped over the grain boundaries to be small, and hence the contrast low.

3.4.2. R-EBIC of $\text{CdS}_x\text{Te}_{1-x}$ samples. Figure 14 shows a R-EBIC micrograph of parallel $\Sigma = 3$ twin boundaries in $\text{CdS}_x\text{Te}_{1-x}$. It shows contrast with bright \rightarrow dark sense; no other types were seen. This contrast is consistent with upward band bending at the twin boundaries.

3.4.3. R-EBIC discussion. As described in the introduction, the sense of grain boundary band bending within a solar cell absorber layer is important in governing electrical passivation. In these R-EBIC experiments dark \rightarrow bright contrast for CdTe and bright \rightarrow dark contrast for $\text{CdS}_x\text{Te}_{1-x}$ (consistent with downward and upward band bending, respectively) have been observed. By combining these observations with experimental observations of (i) diffusion of CdS along grain boundaries from the heterojunction side in the CdTe in solar cells, and (ii) enrichment of the CdTe grain boundaries from back side with Te during processing, mechanisms for grain boundary passivation in these cells may be postulated: presuming the CdTe to have downward band bending in its as-deposited state, this is not favourable for photocurrent collection. Passivation arises from two sources: (i) formation of $\text{CdS}_x\text{Te}_{1-x}$ at the grain boundaries causes them to be associated with upward bending bands—these repel minority carrier electrons, and (ii) formation of Te at the CdTe grain boundaries acts to reduce downward band bending.

However, these mechanisms may be only partly responsible for passivation—there is evidence from DLTS [34]

and EBIC [35] that grain boundary passivation is at least partly mediated by the ubiquitous CdCl_2 processing.

To conclude this discussion, the form of the potential deduced here for $\text{CdS}_x\text{Te}_{1-x}$ shall be compared with the models for grain boundary potentials shown in figure 2. The model due to Galloway (figure 2(b)) is identical to the present one and is itself inferred from electron beam measurements. The Woods model (figure 3(a)) shows upward band bending shielding a region of downward band bending that is not revealed by the electron beam methods. Woods electrical measurements do not give an indication of lateral scale. It is therefore possible that the two models are consistent, and the differences between them arise from the limits of the electron beam (the beam spreading of a 20 keV electron beam in CdTe is $\sim 1 \mu\text{m}$).

4. Conclusions

4.1. Crystal growth aspects

The SSVG method was successful in forming small single grained (but twinned) crystals of $\text{CdS}_x\text{Te}_{1-x}$ ($x \approx 0.067$) and with uniformity 1–2% of the value of x . In its present form, the SSVG method has proved suitable for the research scale growth of ternary crystals formed from binaries having disparate vapour pressures. As expected from lattice stability criteria, this low x composition of $\text{CdS}_x\text{Te}_{1-x}$ is pre-disposed to twinning and the twin : matrix fraction of the boule examined was equal to within the accuracy of the measurement. Study of the morphology and distribution of the twins lead to a discussion of both the origin of twins and the mechanism of progressive grain size increase during the continuous SSVG process: clustering of the twin boundaries and the absence of large grains is consistent with the following scheme: twins and grains are nucleated at seeds in the granular source material. Interface energy-driven grain growth causes high energy grain boundaries to be eliminated but not straight, low energy twin boundaries. Twin boundary clustering is consistent with multiple nucleation in certain seed grains. Deformation twinning was considered unlikely as growth was free from the walls of the container.

4.2. Solar cell aspects

The R-EBIC contrast effects observed at extended defects in CdTe and $\text{CdS}_x\text{Te}_{1-x}$ are consistent with the following:

- (a) CdTe: high angle grain boundaries, lateral and coherent twin boundaries and sub-grain boundaries (dislocation walls) display downward band bending. The extent of this is reduced near to Te inclusions where they decorate high energy boundaries.
- (b) $\text{CdS}_x\text{Te}_{1-x}$: twin boundaries were investigated and show upward band bending.

The possible implications for CdTe/CdS solar cells are as follows: in its as-deposited state, the grain boundaries in the CdTe trap minority carrier electrons and recombination loss is strong. Processing of the material has two effects. Firstly, the CdTe grain boundary interfaces near the contact surface are enriched with Te. By analogy with the behaviour of Te inclusions at grain boundaries, this could act to

reduce the recombination loss. Secondly, the processing promotes diffusion of CdS into the grain boundaries near the heterojunction, making their composition CdS_xTe_{1-x} (where $x < 0.2$, the approximate solubility limit). By analogy with bulk CdS_xTe_{1-x} such grain boundaries will repel minority carriers. If operative, it can be said that these mechanisms are expected to provide only part of the grain boundary passivation—it is known that CdCl₂ processing also plays a role [25].

Acknowledgments

This work was part funded by KBN grant 7 T08A 006 20. The authors would like to thank James Sadler for assistance in sample preparation and Mike Cousins of Cranfield University for useful discussions on grain growth.

References

- [1] Ohata K, Saraie J and Tanaka T 1973 *Japan. J. Appl. Phys.* **12** 1198–204
- [2] Wood D A, Rogers K D, Lane D W, Conibeer G J and Parton D 1998 *J. Mater. Sci. Lett.* **17** 1511–14
- [3] Ohata K, Saraie J and Tanaka T 1973 *Japan. J. Appl. Phys.* **12** 1641
- [4] Jensen D G, McCandless B E and Birkmire R W 1996 *Proc. Mat. Res. Soc. Symp.* **426** 325
- [5] Roh J S and Im H B 1988 *J. Mater. Sci.* **23** 2267–72
- [6] McCandless B E and Birkmire R W 2000 Diffusion in CdS/CdTe thin film couples *16th PVSEC (Glasgow)* (WIP) p 349
- [7] Lane D W, Conibeer G J, Wood D A, Rogers K D, Capper P, Romani S and Hearne S 1999 *J. Cryst. Growth* **197** 743–8
- [8] Szczerbakow A, Domagala J, Rose D, Durose K, Ivanov V Y and Omeltchouk A 1998 *J. Cryst. Growth* **191** 673
- [9] Szczerbakow A 2001 *Cryst. Growth Design* **1** 183–5
- [10] Szczerbakow A, Domagala J, Golacki Z, Ivanov V Y and Leszczynski M 1998 *Cryst. Res. Technol.* **33** 875
- [11] Szczerbakow A, Domagala J, Golacki Z and Swiatek K 1999 *Cryst. Res. Technol.* **34** 53
- [12] Goldfinger P and Jeunehomme M 1963 *Trans. Faraday Soc.* **59** 2851
- [13] Durose K 1996 Trends in structural defects in narrow-gap II-VI compounds *Narrow-gap II-VI Compounds for Opto-Electronic and Electro-magnetic Applications* ed P Capper (London: Chapman and Hall)
- [14] Holt D 1964 *J. Phys. Chem. Solids* **25** 1385
- [15] Durose K, Russell G J and Woods J 1985 *Inst. Phys. Conf. Ser.* **76** 233
- [16] Yeh C Y, Lu Z W, Froyen S and Zunger A 1992 *Phys. Rev. B: Condens. Matter* **46** 10086–97
- [17] Durose K, Sadler J R E, Yates A J W and Szczerbakow A 2000 R-EBIC study of the electrical activity of grain boundaries in CdTe and Cd(S,Te) *28th IEEE Photovoltaic Specialists Conf. (Anchorage, Alaska, USA)* (Piscataway, NJ: IEEE) p 487
- [18] Hurlle D T J 1995 *J. Cryst. Growth* **147** 239–50
- [19] Voronkov V 1975 *Sov. Phys.-Cryst.* **19** 573
- [20] Cutter J R and Woods J 1979 *J. Cryst. Growth* **47** 405–13
- [21] Vere A W, Cole S and Williams D J 1983 *J. Electronic Mater.* **12** 551–61
- [22] Woods L M, Levi D H, Kaydanov V, Robinson G Y and Ahrenkiel R K 1998 Electrical characterisation of CdTe grain-boundary properties from as-processed CdTe/CdS solar cells *2nd World Conf. Exhibition on Photovoltaic Solar Energy Conversion (Vienna)* (Glasgow: WIP) p 1043
- [23] Woods L M, Robinson G Y and Levi D H 2000 The effects of CdCl₂ on CdTe electrical properties using a new theory for grain boundary conduction *28th IEEE Photovoltaic Specialists Conf. (Anchorage, Alaska, USA)* (Piscataway, NJ: IEEE) pp 603–6
- [24] Galloway S A, Edwards P R and Durose K 1999 *Solar Energy Materials and Solar Cells* **57** 61–74
- [25] Edwards P R, Galloway S A and Durose K 2000 *Thin Solid Films* **372** 284–91
- [26] Russell J D and Leach C 1995 *J. Eur. Ceram. Soc.* **15** 617–22
- [27] Holt D B, Raza B and Wojcik A 1996 *Mater. Sci. Eng. B* **42** 14–23
- [28] Inoue M, Teramoto I and Takayanagi S 1962 *J. Appl. Phys.* **33** 2578–81
- [29] Durose K, Russell G J and Woods J 1985 *J. Cryst. Growth* **72** 85
- [30] Magnea N and Pautrat J L 1994 Luminescence of CdTe, CdZnTe and CdSeTe *Properties of Narrow Gap Cadmium-based Compounds* ed P Capper (London: IEE/INSPEC)
- [31] Mullin J B 2002 Personal communication
- [32] Cousins M 2001 Microstructure of absorber layers in CdTe/CdS solar cells *PhD thesis* Department of Physics, University of Durham, Durham
- [33] Durose K, Cousins M A, Boyle D S, Beier J and Bonnet D 2002 *Thin Solid Films* **403–404** 369–404
- [34] Laurencio M A, Wai Lek N, Homewood K P and Durose K 1999 *Appl. Phys. Lett.* **75** 277
- [35] Edwards P R, Halliday D P, Durose K, Richter H and Bonnet D 1997 The influence of CdCl₂ treatment and interdiffusion on grain boundary passivation in CdTe/CdS solar cells *14th Photovoltaic Solar Energy Conf. (Barcelona)* (Glasgow: WIP) p 2083